Cyclophilin D controls mitochondrial pore–dependent Ca^{2+} exchange, metabolic flexibility, and propensity for heart failure in mice

John W. Elrod,[1] Renee Wong,[2] Shikha Mishra,[3] Ronald J. Vagnozzi,[4] Bhuvana Sakthievel,[5] Sanjeewa A. Goonasekera,[1] Jason Karch,[1] Scott Gabel,[2] John Farber,[5] Thomas Force,[4] Joan Heller Brown,[3] Elizabeth Murphy,[2] and Jeffery D. Molkentin[1]

[1]Department of Pediatrics, University of Cincinnati, Cincinnati Children's Hospital Medical Center, Howard Hughes Medical Institute, Cincinnati, Ohio, USA. [2]Translational Medicine Branch, National Heart, Lung, and Blood Institute, NIH, Bethesda, Maryland, USA. [3]Department of Pharmacology, University of California, San Diego, La Jolla, California, USA. [4]Center for Translational Medicine and Cardiology Division and [5]Department of Pathology, Thomas Jefferson University, Philadelphia, Pennsylvania, USA.

Cyclophilin D (which is encoded by the *Ppif* gene) is a mitochondrial matrix peptidyl-prolyl isomerase known to modulate opening of the mitochondrial permeability transition pore (MPTP). Apart from regulating necrotic cell death, the physiologic function of the MPTP is largely unknown. Here we have shown that *Ppif*$^{-/-}$ mice exhibit substantially greater cardiac hypertrophy, fibrosis, and reduction in myocardial function in response to pressure overload stimulation than control mice. In addition, *Ppif*$^{-/-}$ mice showed greater hypertrophy and lung edema as well as reduced survival in response to sustained exercise stimulation. Cardiomyocyte-specific transgene expression of cyclophilin D in *Ppif*$^{-/-}$ mice rescued the enhanced hypertrophy, reduction in cardiac function, and rapid onset of heart failure following pressure overload stimulation. Mechanistically, the maladaptive phenotype in the hearts of *Ppif*$^{-/-}$ mice was associated with an alteration in MPTP-mediated Ca^{2+} efflux resulting in elevated levels of mitochondrial matrix Ca^{2+} and enhanced activation of Ca^{2+}-dependent dehydrogenases. Elevated matrix Ca^{2+} led to increased glucose oxidation relative to fatty acids, thereby limiting the metabolic flexibility of the heart that is critically involved in compensation during stress. These findings suggest that the MPTP maintains homeostatic mitochondrial Ca^{2+} levels to match metabolism with alterations in myocardial workload, thereby suggesting a physiologic function for the MPTP.

Introduction

Opening of the mitochondrial permeability transition pore (MPTP) is critically involved in regulating cell death by inducing a sustained and irreversible loss of inner mitochondrial membrane potential, coinciding with mitochondrial swelling and rupture (1). The proteins that constitute the MPTP, localized between the inner and outer mitochondrial membranes, remain unknown. Cyclophilin D (CypD), a mitochondrial matrix peptidyl-prolyl *cis-trans* isomerase, stands as the only genetically verified component of the MPTP that functions in gating the pore (2–5). Cyclosporine A (CsA) and its analogs inhibit CypD, leading to desensitization of MPTP opening and reduced necrotic cell death following Ca^{2+} overload or reactive oxygen species stimulation (6–8). Genetic deletion of *Ppif* (the gene encoding CypD) in the mouse demonstrates that MPTP opening is critically involved in long-term degenerative diseases such as muscular dystrophy, Alzheimer disease, Parkinson disease, and multiple sclerosis, as well as acute cellular loss following myocardial infarction and stroke (3, 4, 9–11). While such translational studies clearly demonstrate that the MPTP functions as a final mechanism for cellular necrosis in various pathologic states, the baseline or homeostatic function of the MPTP in healthy cells remains largely unknown, although regulation of mitochondrial matrix Ca^{2+} levels has been suggested (12–14). The heart is an ideal organ system for evaluating the potential physiologic function of the MPTP, given that mitochondria constitute approximately one-third the volume of an adult cardiomyocyte and the intimate dependence of the heart on Ca^{2+} and high-energy phosphate production at all times.

Given that loss of CypD benefits the heart acutely following myocardial ischemia-reperfusion injury by preventing necrotic cell death, we initially hypothesized that *Ppif*$^{-/-}$ mice would fare better in heart failure, especially since the development of heart failure is associated with a cumulative loss of myocytes over time that is thought to contribute to dysfunction (15, 16). However, in direct contrast to our hypothesis, we observed that *Ppif*$^{-/-}$ mice were more susceptible to heart failure initiated by several stimuli, including physiologic exercise-induced hypertrophy, and that this progressive myocardial dysfunction was not associated with changes in myocardial cell death rates as analyzed by histology and TUNEL staining. These surprising results laid the groundwork for the current study, wherein we propose a model for the physiologic function of the mitochondrial permeability pore independent of its well-regarded role in cell death.

Results

Baseline characterization and aging phenotype of Ppif$^{-/-}$ *mice.* Mice null for the *Ppif* gene (CypD protein) displayed normal LV dimension

Authorship note: John W. Elrod and Renee Wong contributed equally to this work.
Conflict of interest: The authors have declared that no conflict of interest exists.
Citation for this article: *J Clin Invest.* 2010;120(10):3680–3687. doi:10.1172/JCI43171.

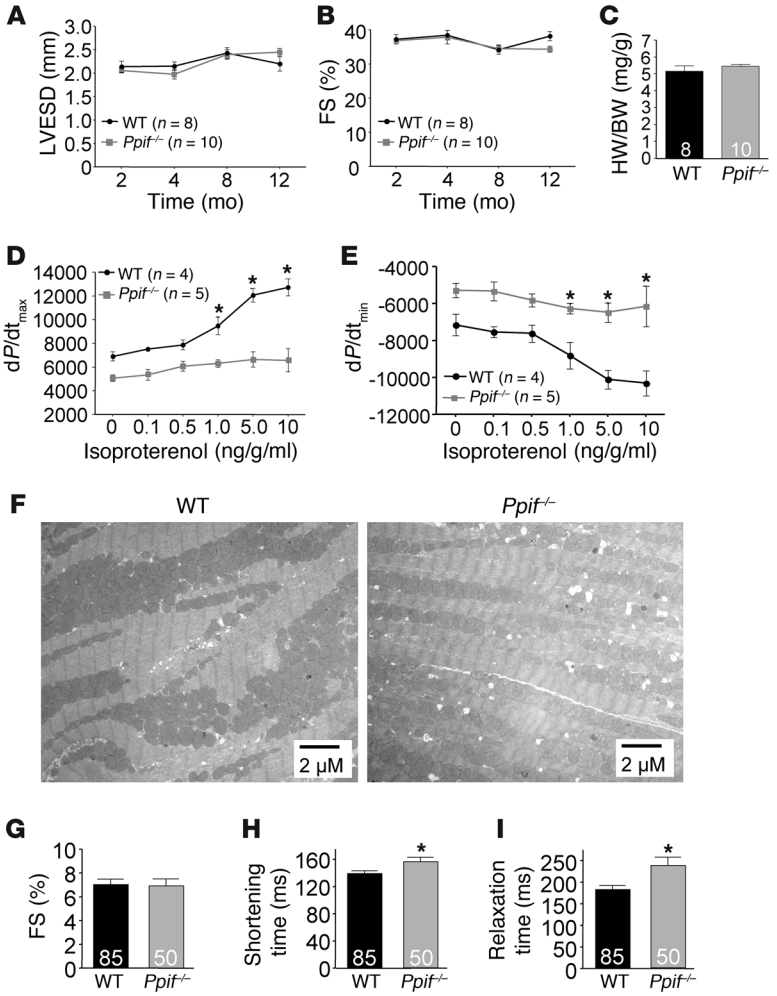

Figure 1
Baseline characterization and aging of *Ppif*$^{-/-}$ mice. (**A**) WT and *Ppif*$^{-/-}$ mice were evaluated from 2 months to 1 year of age for changes in LV end-systolic dimension (LVESD). (**B**) LV percent fractional shortening (FS) from 2 to 12 months of age. (**C**) Heart weight to body weight (HW/BW) ratio in mice 12 months of age. (**D**) LV contractility (dP/dt_{max}) in mice 8 months of age following isoproterenol dose escalation. (**E**) LV relaxation (dP/dt_{min}) in mice 8 months of age following isoproterenol dose escalation. (**F**) Representative electron micrographs of sarcomeric and mitochondrial structure in LV heart histological sections. (**G**) FS (%) in isolated adult cardiomyocytes paced at 0.5 Hz. (**H**) Shortening time (50% time from peak) of isolated adult cardiomyocytes. (**I**) Relaxation time (50% time from peak) of isolated adult cardiomyocytes. All values are reported as mean ± SEM. Sample size for each group is indicated inside the respective bar. *$P < 0.05$ versus WT.

and performance measured by echocardiography at 2, 4, 8, and 12 months of age (Figure 1, A and B). There was also no difference in heart weights of mice at 12 months of age, nor any defects in myofilament or mitochondrial architecture, as assessed by transmission electron microscopy (Figure 1, C and F). However, while baseline contractility did not differ between WT and *Ppif*$^{-/-}$ mice at 8 months of age, maximum contractile reserve, revealed by infusion of isoproterenol (a β-adrenergic receptor agonist), was compromised in *Ppif*$^{-/-}$ mice (dP/dt_{max}, Figure 1D), as was relaxation (dP/dt_{min}, Figure 1E). To determine whether the observed myocardial dysfunction was myocyte specific, we examined sarcomeric shortening and cytosolic Ca^{2+} transients in isolated adult cardiomyocytes. While the baseline percent fractional shortening was comparable to that in WT myocytes, the shortening time and relaxation time were significantly increased in *Ppif*$^{-/-}$ myocytes (Figure 1, G–I), consistent with our in vivo findings. In addition, cytosolic Ca^{2+} transients from adult *Ppif*$^{-/-}$ cardiomyocytes showed a longer time of decay, substantiating the observed increase in relaxation time (Supplemental Figure 1; supplemental material available online with this article; doi:10.1172/JCI43171DS1).

Ppif$^{-/-}$ *mice are more susceptible to myocardial hypertrophy and heart failure following pressure overload.* To explore this maladaptive phenotype further, we subjected *Ppif*$^{-/-}$ mice to stress stimulation as a means of unmasking underlying problems associated with a loss in functional reserve. Indeed, *Ppif*$^{-/-}$ mice were unable to compensate for the increase in afterload caused by transaortic constriction (TAC), displaying a 42% reduction in fractional shortening at the 6-week time point as compared with WT mice (Figure 2A). *Ppif*$^{-/-}$ mice decompensated within 1 week of TAC stimulation and showed significant ventricular dilation by 2 weeks, with equivalent pressure gradients across the aortic constrictions compared with WT mice (Figure 2, B and C). Consistent with these results, hearts from *Ppif*$^{-/-}$ mice hypertrophied to a greater extent than WT mice after 2 and 6 weeks of TAC stimulation (Figure 2, D and E). Indeed, at the 6-week time point, *Ppif*$^{-/-}$ mice displayed a significantly greater increase (41%) in heart weight normalized to body weight and LV wall thickness compared with WT TAC controls (Figure 2E and Supplemental Table 1), which correlated with approximately the same increase in hypertrophy of individual myocytes in the heart (Figure 2F). Further histological analysis of hearts showed a substantial increase in fibrosis following TAC in *Ppif*$^{-/-}$ mice compared with WT TAC controls (Figure 2G), and indices of congestive heart failure, such as pulmonary edema, were also prominent in *Ppif*$^{-/-}$ animals (Figure 2H). However, we observed no difference in TUNEL-positive nuclei of cardiomyocytes or interstitial cells at 2 and 6 weeks of TAC stimulation in *Ppif*$^{-/-}$ compared with WT hearts, suggesting that the rate of cellular demise was unchanged (Supplemental Figure 2, A–D). The more severe cardiac pathology observed in *Ppif*$^{-/-}$ mice also correlated with stronger activation of the fetal gene program after TAC, including the β–myosin heavy chain gene, atrial natriuretic factor (ANF), and B-type natriuretic peptide (BNP) genes (Figure 2, I–K). Taken together, these results suggest that loss of CypD increases sensitivity to cardiac stress stimulation and disease.

Ppif$^{-/-}$ *mice display increased mortality and heart failure in pathologic and physiologic models of hypertrophy.* To further characterize this maladaptive phenotype due to hypertrophic stimulation, we crossed *Ppif*$^{-/-}$ mice with Ca^{2+}/calmodulin-dependent protein kinase IIδc–transgenic mice (CaMKII-Tg). CaMKIIδc overexpression results in heart failure characterized by a loss of LV function and significant mortality, but more importantly these mice show alterations in intracellular Ca^{2+} handling and a predisposition to increased

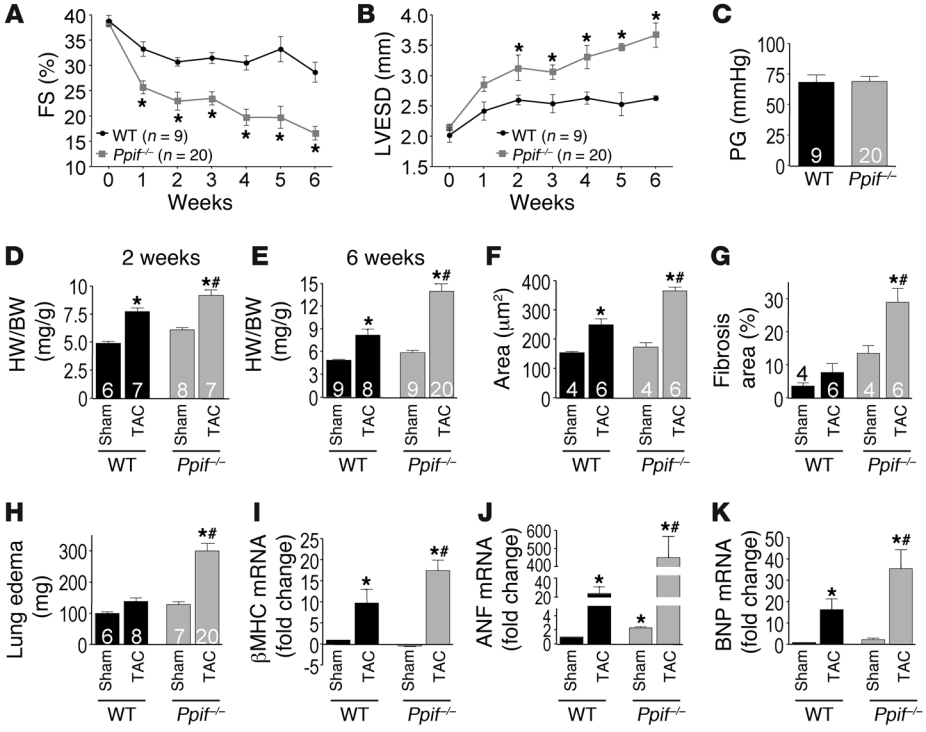

Figure 2

Ppif$^{-/-}$ mice rapidly develop hypertrophy and heart failure following pressure overload. (**A**) LV percent FS following TAC in WT and *Ppif*$^{-/-}$ mice. (**B**) LVESD following TAC. (**C**) Pressure gradients (PG) across the TAC 1 week after TAC. (**D**) HW/BW ratio 2 weeks following TAC or sham operation. (**E**) HW/BW ratio 6 weeks following TAC. (**F**) Cardiomyocyte cross-sectional area (μm^2) after TAC in LV histological sections. (**G**) Morphometric analysis of fibrotic area in heart histological sections after TAC (percent blue area in Mason's trichrome–stained hearts). (**H**) Lung edema (wet weight in mg – dry weight in mg) 6 weeks following TAC. (**I**) βMHC (encoded by the *Myh7* gene) mRNA expression following TAC (fold change versus WT sham, n = 4/group). (**J**) ANF (*Nppa* gene) mRNA expression following TAC (fold change versus WT sham, n = 4/group). (**K**) BNP (*Nppb* gene) mRNA expression following TAC (fold change versus WT sham, n = 4/group). All values are reported as mean ± SEM. Sample size for each group is indicated inside the respective bar. $^*P < 0.05$ versus WT (**A** and **B**) or sham (**D**–**K**); $^{\#}P < 0.05$ versus WT TAC.

mitochondrial Ca^{2+} (17–19). As will be presented in figures below, this predisposition to elevated mitochondrial Ca^{2+} with CaMKIIδc overexpression is similar to alterations observed in *Ppif*$^{-/-}$ hearts, making the cross mechanistically germane. Indeed, hypertrophy associated with the CaMKII-Tg was synergistically increased when mice were crossed into the *Ppif*$^{-/-}$ background, and the cross also resulted in earlier lethality (Figure 3, A and B). Importantly, isolation of mitochondria from the hearts of these crossed mice showed that MPTP formation after Ca^{2+} stimulation was inhibited by genetic loss of *Ppif*, even with the CaMKII-Tg (Figure 3C).

The rapid onset of cardiac decompensation in *Ppif*$^{-/-}$ mice after TAC stimulation coupled with their inability to even modestly increase cardiac contractility following acute β-adrenergic stimulation suggested a loss in functional reserve. To address this possibility, and minimize the confounding effect of a pathologic insult, we subjected *Ppif*$^{-/-}$ mice to swimming exercise to induce physiologic hypertrophy. Remarkably, swimming resulted in significant mortality, with more than 40% of *Ppif*$^{-/-}$ mice having died by the conclusion of the training period due to extreme fatigue and drowning (Figure 3D). Histological analysis showed no overt pathology, including no induction of cell death (Supplemental Figure 2, E and F, and data not shown). Swimming also induced significantly greater cardiac hypertrophy and pulmonary edema in *Ppif*$^{-/-}$ mice as compared with WT controls, suggesting an inability to compensate for the higher workload (Figure 3, E and F). In total, these results suggest that loss of CypD compromises the functional reserve of the heart and renders it more susceptible to failure, even with physiologic stimulation that is normally cardioprotective.

Cardiac-restricted transgenic rescue of Ppif$^{-/-}$ *pathology following TAC.* We hypothesized that the extreme predisposition to decompensation in *Ppif*$^{-/-}$ mice with stress stimulation was due to a defect in mitochondrial function within myocytes themselves. However, *Ppif*$^{-/-}$ mice lack the gene in all cells; hence, it was formally possible that the cardiac defect observed was not myocyte autonomous. To address this issue, we crossed transgenic mice expressing CypD under control of the α–myosin heavy chain promoter (CypD-Tg) into the *Ppif*$^{-/-}$ background. Western blotting demonstrated that *Ppif*$^{-/-}$ mice lacked CypD protein in the heart, while CypD-Tg × *Ppif*$^{-/-}$ crossed mice had restored myocyte CypD protein, albeit to levels slightly higher than in the WT control (Figure 4A). After 3 weeks of TAC stimulation, *Ppif*$^{-/-}$ mice from the same backcross again showed rapid loss of ventricular performance, greater increases in cardiac hypertrophy, and pulmonary edema, all of which were rescued back to WT levels by the CypD-Tg cross (Figure 4, B, C, and D). Importantly, pressure gradients across the aortic constriction did not differ among the groups (Figure 4E). These results suggest that the maladaptive cardiac phenotype observed in *Ppif*$^{-/-}$ mice is myocyte dependent.

Ppif$^{-/-}$ *mice display substantial metabolic reprogramming.* To further examine the mechanism whereby CypD loss from cardiac mitochondria sensitizes to failure, we performed a genome-wide array using mRNA isolated from LV tissue of 8-week-old WT and *Ppif*$^{-/-}$ mice. Affymetrix gene array analysis revealed that 362 probe sets were significantly different (ANOVA, $P < 0.01$), with a minimum difference in gene expression of 25% (Figure 5A). Unbiased functional annotation revealed numerous metabolism-associated gene groups that were significantly enriched, suggesting an alteration in mitochondrial function (Table 1). To examine this possible mechanism further, we evaluated substrate utilization in a working heart preparation with ^{13}C NMR spectrometry. The analysis showed that *Ppif*$^{-/-}$ hearts had a significant increase in the glucose to palmitate ratio, suggesting a metabolic shift away from fatty acid oxidation toward glycolysis (Figure 5B). We also observed an increase in the succinate to glutamate ratio in *Ppif*$^{-/-}$ hearts,

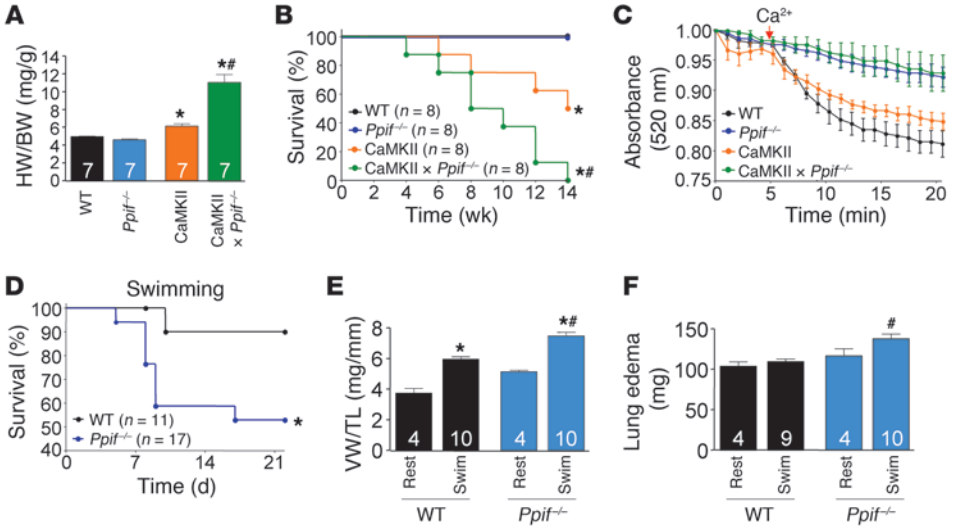

Figure 3

Ppif$^{-/-}$ mice display increased mortality and heart failure in pathologic and physiologic models of hypertrophy. (**A**) HW/BW ratios in the indicated groups of mice at 4 weeks of age. (**B**) Kaplan-Meier survival plot in the groups of mice shown. (**C**) Mitochondrial swelling following Ca^{2+} addition (indicated by red arrow), measured as change in absorbance (520 nm) over time (representative tracing of 3 independent experiments). (**D**) Kaplan-Meier survival plot during swimming exercise. (**E**) Ventricular weight/tibia length (VW/TL) ratios in mice at completion of the swimming protocol. (**F**) Lung edema (wet weight in mg – dry weight in mg) at completion of the swimming protocol. All values are reported as mean ± SEM. Sample size for each group is indicated inside the respective bar. $^{*}P < 0.05$ versus WT control (**A**, **B**, and **D**) or rested group (**E**); $^{\#}P < 0.05$ versus CaMKII and *Ppif*$^{-/-}$ (**A**–**C**) or versus WT swim (**E** and **F**).

and while the significance of this change is uncertain, it does suggest increased TCA cycle flux (Figure 5C). Associated with these changes in substrate utilization, the activities of pyruvate dehydrogenase (PDH) and α–ketoglutarate dehydrogenase (αKGD), two Ca^{2+}-regulated mitochondrial enzymes with rate-limiting metabolic properties, were significantly enhanced in *Ppif*$^{-/-}$ hearts (Figure 5, D and E). Importantly, protein expression levels for the PDH subunits did not differ between WT and *Ppif*$^{-/-}$ hearts, nor were expression levels for αKGD and two other Ca^{2+}-regulated mitochondrial dehydrogenases changed (Figure 5, F and G), suggesting that the increase in activity was due to increased mitochondrial Ca^{2+}.

Ppif$^{-/-}$ *mice display altered mitochondrial* Ca^{2+} *exchange.* Given the observed metabolic changes and increased αKGD and PDH activity, we suspected an increase in mitochondrial matrix Ca^{2+}. Indeed, we previously showed that mitochondria from *Ppif*$^{-/-}$ mice take up more Ca^{2+} before undergoing MPTP formation (3). Reexamination of this phenomenon with purified mitochondria from *Ppif*$^{-/-}$ mice showed nearly 3-fold-greater Ca^{2+} accumulation prior to MPTP opening compared with that in WT mitochondria (Figure 6A). More importantly, direct measurement of total mitochondrial Ca^{2+} content of *Ppif*$^{-/-}$ hearts showed a 2.6-fold elevation compared with WT mitochondria (Figure 6B). Taken together, these results suggest that in the absence of CypD mitochondrial matrix Ca^{2+} levels are reset and constitutively elevated, consistent with the observed metabolic alterations.

We hypothesized that the elevated level of matrix Ca^{2+} observed in mitochondria from hearts of *Ppif*$^{-/-}$ mice was due to reduced physiological opening of the MPTP, as its low conductance state has been implicated in affecting Ca^{2+} homeostasis (20, 21). To address this hypothesis, we used cultured neonatal rat ventricular cardiomyocytes infected with an adenovirus encoding a mitochondrial-targeted ratiometric-pericam (mt-pericam) Ca^{2+} sensor pro-

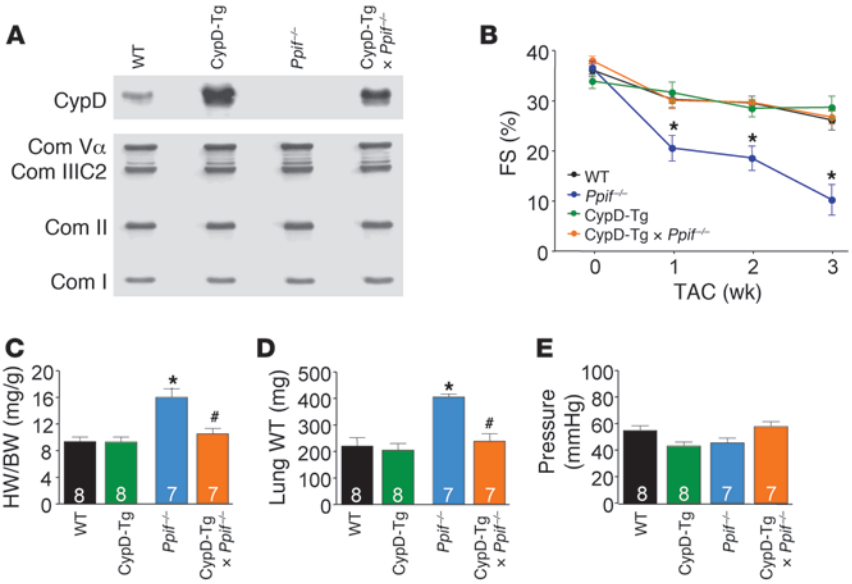

Figure 4

Cardiac-restricted transgenic rescue of *Ppif*$^{-/-}$ pathology following TAC. (**A**) Representative Western blot of CypD and oxidative phosphorylation complexes (Com Vα, III-core 2, II, I) in heart mitochondrial extracts. (**B**) LV percent FS following TAC. (**C**) HW/BW ratio following TAC. (**D**) Lung edema (wet weight in mg – dry weight in mg) following TAC. (**E**) Pressure gradient across the aortic constriction 1 week after TAC. All values are reported as mean ± SEM. Sample size for each group is indicated inside the respective bar. $^{*}P < 0.05$ versus all other groups; $^{\#}P < 0.05$ versus *Ppif*$^{-/-}$ TAC.

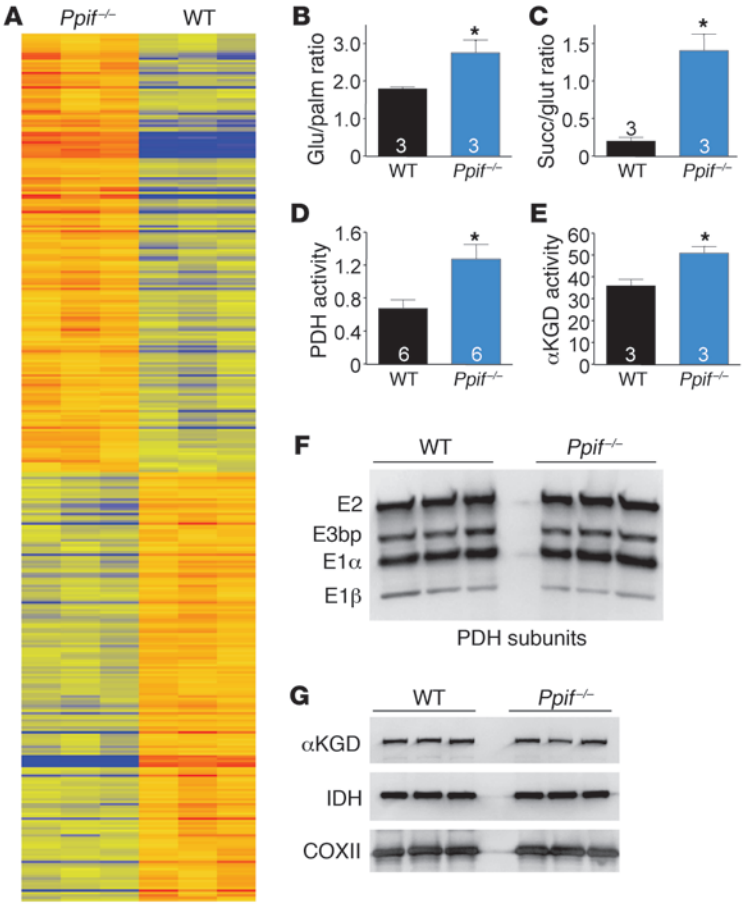

Figure 5

Ppif$^{-/-}$ mice display significant metabolic alterations. (**A**) Heat map displaying gradient differences in gene expression between WT and *Ppif*$^{-/-}$ ventricular tissue at 8 weeks of age (ANOVA, $P < 0.01$). (**B**) Ratio of glucose/palmitate (Glu/palm) consumption in working hearts using ^{13}C NMR spectroscopy. (**C**) Ratio of succinate/cytosolic glutamate (Succ/glut) in working hearts using ^{13}C NMR spectroscopy. (**D**) PDH enzymatic activity in mitochondria isolated from mouse hearts (*y* axis indicates change in mOD/min/mg protein where $r^2 = 1$). (**E**) αKGD enzymatic activity in mitochondria isolated from mouse hearts (rate expressed as nmol NADH/min/mg of protein). (**F**) Western blot of PDH complex expression. (**G**) Western blot of αKGD and isocitrate dehydrogenase (IDH); mitochondrial cytochrome oxidase subunit II (COXII) was used as a loading control. *$P < 0.05$ versus WT.

tein (22). This system permits direct measurement of mitochondrial matrix Ca^{2+} levels in real time and, in conjunction with CsA, allowed examination of MPTP-dependent Ca^{2+} handling effects. In agreement with previous reports, we found mt-pericam to be exclusively expressed in mitochondria (data not shown) (22). Following a single 80-V pulse, CsA-treated myocytes showed a significantly greater mitochondrial Ca^{2+} transient compared with untreated myocytes (Figure 6C). Quantification of this effect in multiple independent myocytes showed a quantitative increase in the amplitude of the Ca^{2+} transient, decreased rise time, and increased rise slope (Figure 6, D and E, and data not shown). We also performed continuous pacing (80 v, 0.2 Hz, 100 seconds) to allow greater mitochondrial matrix Ca^{2+} accumulation for examining extrusion dynamics. Under paced conditions, MPTP desensitization with CsA also decreased the rise time in Ca^{2+} accumulation, but more importantly, it prolonged the recovery time after pacing (Figure 6, F and G). Both of these effects are consistent with a proposed homeostatic function of the MPTP as a Ca^{2+} "leak" or release channel to prevent Ca^{2+} overload in cardiac mitochondria.

Discussion

CypD inhibition is known to allow greater accumulation of mitochondrial Ca^{2+} in vitro, yet the mechanism proposed for this phenomenon has always been tied to cell death. However, our data taken together with past studies suggest a critical role for CypD and the MPTP in controlling mitochondrial Ca^{2+} homeostasis for proper metabolic function. For example, past in vitro studies suggested that transient opening of the MPTP might allow the exchange of matrix Ca^{2+} across the inner membrane without causing cellular demise. Evidence for this hypothesis emerged in 1992 in a study by Altschuld and colleagues, who showed that CsA increased mitochondrial Ca^{2+} loading and inhibited efflux in isolated rabbit cardiomyocytes (23). This hypothesis was extended by Ichas et al., who presented a biophysical model of Ca^{2+}-induced mitochondrial Ca^{2+} release that involved low-conductance MPTP opening for mitochondrial Ca^{2+} efflux (20). Similarly, Siemen and colleagues used mitoplasts and direct patching to examine MPTP opening in the mitochondrial membrane. They showed a large conductance current, with multiple subconductance states, that was Ca^{2+} activated and reversibly inhibited with CsA (24). Our results extend this Ca^{2+} homeostasis model by showing that genetic loss of CypD results in mitochondria with higher resting Ca^{2+} levels in the heart and that CsA treatment acutely reduces mitochondrial Ca^{2+} efflux and leak in cultured cardiomyocytes.

In the current study, we provide in vivo evidence linking MPTP-mediated Ca^{2+} efflux to global changes in metabolic substrate utilization, a mechanism that appears crucial to the heart's ability to maintain contractility in response to increased workload (25). For example, increases in cardiac contractility are tied to greater intracellular Ca^{2+} cycling rates in myocytes, which has the net effect of enhancing mitochondrial Ca^{2+} load through the Ca^{2+} uniporter (MCU). Mitochondrial extrusion rates through the mitochondrial Na^+/Ca^{2+} exchanger or other transporters/channels lag behind the cytoplasmic Ca^{2+} transient, resulting in accumulation of Ca^{2+} at higher beating rates until physiologic opening of the MPTP occurs. The net increase in mitochondrial Ca^{2+} leads to activation of 3 mitochondrial dehydrogenases important in substrate utilization and oxidative metabolism, thereby increasing energy supply during increased workloads (26). Indeed, simultaneous measurements of mitochondrial Ca^{2+} and NADH have correlated increased mitochondrial Ca^{2+} load with increased oxidative phosphorylation and ATP production (27). Moreover, pharmacologic inhibition of the MCU reduced the activity of the aforementioned intra-mitochondrial dehydrogenases by reducing Ca^{2+} influx (28, 29). Analogous to this model, we found enhanced enzymatic activity for PDH and αKGD at baseline in *Ppif*$^{-/-}$ hearts, consistent with the finding of increased basal Ca^{2+} in the mitochondrial matrix.

Table 1
Ppif$^{-/-}$ hearts display significant metabolic reprogramming

Functional group	*P*	Fold enrichment
Pigment biosynthetic process	6.94×10^{-4}	12.18
Pigment metabolic process	1.40×10^{-3}	10.15
Secondary metabolic process	5.81×10^{-3}	6.89
Porphyrin biosynthesis	6.73×10^{-3}	23.44
Heme biosynthesis	8.34×10^{-3}	21.09
Cellular metabolic process	7.14×10^{-3}	1.19
Metabolic process	1.64×10^{-2}	1.15
Primary metabolic process	2.13×10^{-2}	1.16
Amino acid catabolic process	3.22×10^{-2}	5.73
Di-, tri-valent inorganic cation transport	5.36×10^{-3}	3.77
Cation transmembrane transporter activity	2.85×10^{-2}	1.95
Substrate-specific transmembrane transporter activity	4.97×10^{-2}	1.63

DAVID functional annotation microarray analysis of gene class changes in *Ppif*$^{-/-}$ hearts, which showed many alterations in mitochondrial genes and genes involved in metabolism.

PDH in particular is central in linking glycolysis to the citric acid cycle by converting pyruvate to acetyl-CoA. We hypothesize that the mitochondrial calcium-mediated increase in PDH activity may account for the observed elevation in glucose oxidation. For example, inhibition of PDH kinase, which increases PDH activity, enhances glucose oxidation in rat heart (30).

Increased basal Ca^{2+} in the mitochondria mimics higher contractile workloads, which on the surface would not appear to be detrimental, likely explaining why *Ppif*$^{-/-}$ mice are relatively unaffected when not stressed. However, our working hypothesis is that such a state of constitutively higher intramitochondrial Ca^{2+} reduces the dynamic range in cardiac metabolism, ultimately decreasing the heart's metabolic reserve capacity and rendering it more sensitive to decompensation with even subtle stress provocation (such as sustained exercise). At first glance, these results seem contrary to our previous report that *Ppif* deletion rescued heart disease in β2a-Tg mice, a transgenic model with severe heart failure due to massive Ca^{2+} overload and myocyte necrosis (31). However, the loss of *Ppif* in β2a-Tg mice was likely protective, blocking the pathologic function of the MPTP in its large-conductance state and secondary myocyte necrosis, hence predominating over the physiologic function of the MPTP in regulating mitochondrial matrix Ca^{2+}.

A hallmark of pathologic hypertrophy is metabolic reprogramming back toward a fetal-like gene program, favoring glycolysis over fatty acid oxidation (32). While this metabolic reprogramming was originally postulated to be compensatory, studies in genetically modified mouse models predict that any switching of major metabolic substrate utilization in the heart is detrimental (16, 33). For example, *Ppara*$^{-/-}$ mice display an increase in glucose oxidation and a decrease in fatty acid oxidation resulting in myocardial fibrosis and an inability to tolerate increased workloads (34–36). In parallel, *Ppard*$^{-/-}$ (PPARγ protein) mice display increased glucose uptake, with a decrease in fatty acid β-oxidation and likewise exhibit systolic dysfunction and the rapid onset of heart failure (37). Even more striking, a recent attempt to genetically overcome a shift in fatty acid utilization by overexpression of Glut1 resulted in vast metabolic reprogramming and myocardial pathology (38). The *Ppif*$^{-/-}$ phenotype strongly fits this paradigm, in that a shift in substrate utilization precedes any overt cardiac pathology, and upon stress-stimulation the observed deficit in metabolic reserve leads to disease.

In conclusion, we have established that CypD and the MPTP represents an important regulator of mitochondrial Ca^{2+} exchange in myocytes that is pivotal in maintaining metabolic plasticity, thereby facilitating adaptation to disease states or increased workload. Thus, our results suggest that the modulation of mitochondrial Ca^{2+} exchange may be an exciting new avenue for the treatment of heart failure.

Methods

Targeted and transgenic mice. The generation of *Ppif*-null mice and CypD-transgenic mice has previously been reported (3). For our experiments, *Ppif*$^{-/-}$ mice were crossed with αMHC-CypD-Tg mice and heterozygous (*Ppif*$^{+/-}$) offspring carrying the CypD transgene crossed with *Ppif*$^{+/-}$ void of the transgene. The offspring of this cross were again mated to generate the 4 genotypes of mice used in the current study: WT, *Ppif*$^{-/-}$, αMHC-CypD-Tg, and *Ppif*$^{-/-}$ × αMHC-CypD-Tg. The generation of CaMKII-Tg mice has previously been reported (17). For our experiments *Ppif*$^{-/-}$ mice were crossed

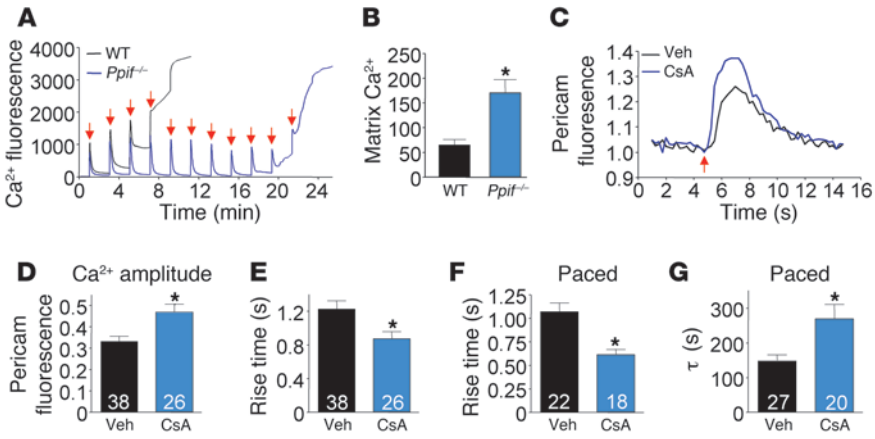

Figure 6
Ppif$^{-/-}$ mice display increased mitochondrial Ca^{2+}. (**A**) Representative tracing of Ca^{2+} uptake in mitochondria isolated from WT and *Ppif*$^{-/-}$ mice (calcium green-5n fluorescence intensity, $485_{excitation}/528_{emission}$; red arrow indicates Ca^{2+} injection). (**B**) Matrix-free Ca^{2+} in mitochondria isolated from ventricular samples (nmol/mg protein). (**C**) Representative tracing from cultured neonatal cardiomyocytes infected with mt-pericam treated with vehicle (Veh) or 1 μM CsA. Pericam fluorescence is the ratio of $490/415_{excitation}$, $530_{emission}$; red arrow indicates field stimulation. (**D**) Amplitude of mitochondrial Ca^{2+} transients in neonatal myocytes following single-pulse stimulation. (**E**) Rise time of mitochondrial Ca^{2+} transients following single-pulse stimulation. (**F**) Average rise time of mitochondrial Ca^{2+} transients during continuous pacing (0.2 Hz for 100 seconds). (**G**) Time decay constant (τ) or recovery to baseline following continuous field stimulation. *$P < 0.05$ versus WT or vehicle.

with CaMKII-Tg mice in the same manner as they were with CypD-Tg. All experiments in the current study utilized littermate controls of matched age and sex. The IACUC of Cincinnati Children's Hospital approved all experiments involving animals.

Western blot analysis. Sample preparation and gel electrophoresis were previously described in detail (39). The following antibodies were used in the current study: CypD (Mitosciences), respiratory chain complexes (OXPHOS blot, Mitosciences), PDH subunits (Mitosciences), αKGD, COX II (Santa Cruz Biotechnologies Inc.), and isocitrate dehydrogenase (Abcam).

Isolation of adult cardiomyocytes, cytosolic Ca^{2+} current, and myocyte shortening. Ventricular myocytes were isolated as described previously (31). Myocytes were maintained at room temperature in 5% CO_2 and 95% O_2 and used within 3 hours of isolation. Myocytes were placed in a chamber mounted on an inverted Nikon microscope and perfused with normal physiological solution (Ringer) containing 2 mM Ca^{2+}. Contractions were measured with video edge detection, and intracellular Ca^{2+} was measured with Fura-2 as described previously (31).

Mitochondria isolation and analysis of mitochondrial Ca^{2+} content. Briefly, the heart was quickly excised and mitochondria isolated in buffers free of EGTA/EDTA, pH 7.4, at 4°C. For measurement of Ca^{2+} content, mitochondria were isolated and washed repeatedly in EGTA/EDTA-free buffers and resuspended in 0.6 N HCl as previously reported (40). Concentration was then determined spectrophotometrically using the *O*-Cresolphthalein Complexone assay (TECO Diagnostics).

Isolated mouse heart preparation and ^{13}C metabolite NMR. Mice were anesthetized with an intraperitoneal injection of 0.10 ml pentobarbital sodium diluted 1:5 in perfusate. The abdominal cavity was exposed with a transverse incision, and 0.05 ml heparin was administered to the inferior vena cava. The heart was quickly isolated and placed in ice-cold Krebs-Henseleit (KH) buffer (25 mM $NaHCO_3$, 120 mM NaCl, 11 mM glucose, 4.7 mM KCl, 1.2 mM KH_2PO_4, 1.2 mM $MgSO_4$, and 1.75 mM $CaCl_2$) to arrest the heart. The heart was perfused via the aorta. A water-filled latex balloon was inserted into the LV to measure hemodynamic parameters using a PowerLab 2/25 and Chart v5.5 software (AD Instruments). All hearts were perfused with KH buffer gassed with 95% O_2 and 5% CO_2 and maintained at 37°C. ^{13}C metabolite labeling was performed as previously described (41). Following equilibration, hearts were perfused in phosphate-free KH buffer with 8 mM glucose, 2 mM 1-^{13}C-glucose, 0.5 mM uniformly labeled ^{13}C-palmitate, and 3% (w/v) BSA for 20 minutes. The hearts were freeze-clamped, extracted with cold 3.6% perchloric acid, and centrifuged at 14,000 *g*. The resulting supernatant was neutralized on ice with 5 M KOH to a pH of approximately 8, centrifuged at 14,000 *g*, and lyophilized. Samples were dissolved in D_2O for ^{13}C NMR measurement, and proton-decoupled ^{13}C spectra were acquired on a Varian Inova 500-MHz NMR spectrometer. By analyzing the scalar coupling pattern of the C-4 carbon resonance of glutamate, we were able to measure the relative contribution of ^{13}C-enriched glucose versus palmitate to the acetyl-CoA pool.

Dehydrogenase activity assays. PDH activity was assayed by using an immunocapture technique and then calculating the mean maximal rate of NADH production (change in mean OD/min where $r^2 = 1$) as described in the manufacturer's instructions (Mitosciences). αKGD activity was monitored using NADH-coupled reactions. Briefly, mitochondria were lysed in 120 mM KCl, 10 mM Tris, 5 mM MOPS, 5 mM KH_2PO_4, and 1% Triton X-100. The homogenate was immediately added to 5 mM $MgCl_2$, 5 mM αKG, 0.2 mM coenzyme A, 0.4 mM thiamine pyrophosphate, and 1 mM NAD^+. NADH produced was measured at an absorbance of 340 nm.

Neonatal myocyte isolation and pericam imaging and analysis. Neonatal rat cardiomyocytes were isolated from Sprague-Dawley rat pups as previously described (42). Cardiomyocytes were allowed to mature for 72 hours in media containing 15% fetal bovine serum. Myocytes were then infected with mt-pericam adenovirus for 6 hours (22). Twenty-four hours following infection, myocytes were utilized in Ca^{2+} experiments. Prior to experiments, myocytes were switched to standard Ringer solution containing 4 mM Ca^{2+}, as previously reported (43). The pericam fluorescence ratio was determined at room temperature using a Delta Scan dual-beam spectrofluorophotometer (Photon Technology International), operated at an emission wavelength of 530 nM, with excitation wavelengths of 490 and 415 nM. The stimulating frequency for Ca^{2+} transient measurements was 0.2 Hz. All data were recorded and analyzed using Chart v5.6 (AdInstruments) and IonWizard (IonOptix) software.

Isolation of mRNA, Taqman qPCR, and gene array. mRNA was isolated using the RNeasy Protect Midi Kit according to manufacturer's instructions (QIAGEN). Reverse transcription was performed in a standard fashion with QuantiTect Reverse Transcription Kit (QIAGEN) supplemented with DNase treatment. Taqman qPCR was carried out according to the manufacturer's instructions using probe sets for αMHC, βMHC, ANP, BNP, and GAPDH. Analysis was carried out using the ΔΔ-CT method with αMHC and GAPDH correction and reported as fold change versus WT sham. Gene expression analysis was performed using Affymetrix Mouse Gene Array 1.0ST. Results were filtered for a raw value greater than 5, followed by ANOVA ($P < 0.01$) statistical analysis of WT versus *Ppif*$^{-/-}$. A raw filter for values greater than 6 was then applied, followed by a volcano plot for WT versus *Ppif*$^{-/-}$ (fold difference >1.25, $P < 0.05$). Results were then analyzed for functional group classification using DAVID functional annotation microarray analysis (http://david.abcc.ncifcrf.gov/home.jsp) (44, 45). The data have been deposited into the Gene Expression Omnibus database (http://www.ncbi.nlm.nih.gov/geo/; accession number GSE23028).

Histology, image analysis, and electron microscopy. For histological analysis, hearts were collected at the indicated times, fixed in 10% buffered formalin, and embedded in paraffin. Serial 5-μm heart sections from each group were stained with H&E and Masson's trichrome (to detect fibrosis). Myocyte cross-sectional areas were analyzed in slides stained with wheat germ agglutinin–FITC conjugate at 50 μg/ml to accurately identify sarcolemmal membrane as previously reported (39). ImageJ (http://rsbweb.nih.gov/ij/) analysis was then performed. All analysis was performed in a blinded fashion. Transmission electron microscopy and TUNEL staining were performed as previously described (11, 39).

Echocardiography, invasive hemodynamics, swimming protocol, and pressure overload. Hypertrophy studies using the TAC model, swimming exercise, and invasive hemodynamics have been previously described (39, 46).

Statistics. All results are presented as mean ± SEM. Statistical analysis was performed using Prism 4.0 (GraphPad Software) for unpaired 2-tailed *t* test (for 2 groups) and 1-way ANOVA with Bonferroni correction (for groups of 3 or more). For experiments performed over time, 2-way ANOVA with Bonferroni post-hoc analysis was used. *P* values less than 0.05 were considered significant.

Acknowledgments

The authors greatly appreciate the technical expertise of Allen York and Michelle Sargent. This work was supported by grants from the NIH to J.W. Elrod (5F32HL092737), J.D. Molkentin (HL62927, HL81104), and to J.H. Brown (HL80101), as well as by an international grant in heart failure research from the Fondation Leducq and the Howard Hughes Medical Institute.

Received for publication March 31, 2010, and accepted in revised form August 4, 2010.

Address correspondence to: Jeffery D. Molkentin, Cincinnati Children's Hospital Medical Center, Howard Hughes Medical Institute, Molecular Cardiovascular Biology, 240 Albert Sabin Way, MLC 7020, Cincinnati, Ohio 45229, USA. Phone: 513.636.3557; Fax: 513.636.5958; E-mail: jeff.molkentin@cchmc.org.

1. Kroemer G, Galluzzi L, Brenner C. Mitochondrial membrane permeabilization in cell death. *Physiol Rev*. 2007;87(1):99–163.
2. Nakagawa T, et al. Cyclophilin D-dependent mitochondrial permeability transition regulates some necrotic but not apoptotic cell death. *Nature*. 2005; 434(7033):652–658.
3. Baines CP, et al. Loss of cyclophilin D reveals a critical role for mitochondrial permeability transition in cell death. *Nature*. 2005;434(7033):658–662.
4. Schinzel AC, et al. Cyclophilin D is a component of mitochondrial permeability transition and mediates neuronal cell death after focal cerebral ischemia. *Proc Natl Acad Sci U S A*. 2005;102(34):12005–12010.
5. Basso E, Fante L, Fowlkes J, Petronilli V, Forte MA, Bernardi P. Properties of the permeability transition pore in mitochondria devoid of Cyclophilin D. *J Biol Chem*. 2005;280(19):18558–18561.
6. Le Quoc K, Le Quoc D. Involvement of the ADP/ATP carrier in calcium-induced perturbations of the mitochondrial inner membrane permeability: importance of the orientation of the nucleotide binding site. *Arch Biochem Biophys*. 1988;265(2):249–257.
7. Halestrap AP, Davidson AM. Inhibition of Ca2(+)-induced large-amplitude swelling of liver and heart mitochondria by cyclosporin is probably caused by the inhibitor binding to mitochondrial-matrix peptidyl-prolyl cis-trans isomerase and preventing it interacting with the adenine nucleotide translocase. *Biochem J*. 1990;268(1):153–160.
8. Bernardi P. The permeability transition pore. Control points of a cyclosporin A-sensitive mitochondrial channel involved in cell death. *Biochim Biophys Acta*. 1996;1275(1–2):5–9.
9. Forte M, et al. Cyclophilin D inactivation protects axons in experimental autoimmune encephalomyelitis, an animal model of multiple sclerosis. *Proc Natl Acad Sci U S A*. 2007;104(18):7558–7563.
10. Du H, et al. Cyclophilin D deficiency attenuates mitochondrial and neuronal perturbation and ameliorates learning and memory in Alzheimer's disease. *Nat Med*. 2008;14(10):1097–1105.
11. Millay DP, et al. Genetic and pharmacologic inhibition of mitochondrial-dependent necrosis attenuates muscular dystrophy. *Nat Med*. 2008;14(4):442–447.
12. Ichas F, Mazat JP. From calcium signaling to cell death: two conformations for the mitochondrial permeability transition pore. Switching from low- to high-conductance state. *Biochim Biophys Acta*. 1998;1366(1–2):33–50.
13. Griffiths EJ. Mitochondrial calcium transport in the heart: physiological and pathological roles. *J Mol Cell Cardiol*. 2009;46(6):789–803.
14. Spat A, Szanda G, Csordas G, Hajnoczky G. High- and low-calcium-dependent mechanisms of mitochondrial calcium signalling. *Cell Calcium*. 2008; 44(1):51–63.
15. Foo RS, Mani K, Kitsis RN. Death begets failure in the heart. *J Clin Invest*. 2005;115(3):565–571.
16. Mudd JO, Kass DA. Tackling heart failure in the twenty-first century. *Nature*. 2008;451(7181):919–928.
17. Zhang T, et al. The deltaC isoform of CaMKII is activated in cardiac hypertrophy and induces dilated cardiomyopathy and heart failure. *Circ Res*. 2003;92(8):912–919.
18. Zhang T, et al. Phospholamban ablation rescues sarcoplasmic reticulum Ca(2+) handling but exacerbates cardiac dysfunction in CaMKIIdelta(C) transgenic mice. *Circ Res*. 2010;106(2):354–362.
19. Sag CM, et al. Calcium/calmodulin-dependent protein kinase II contributes to cardiac arrhythmogenesis in heart failure. *Circ Heart Fail*. 2009;2(6):664–675.
20. Ichas F, Jouaville LS, Mazat JP. Mitochondria are excitable organelles capable of generating and conveying electrical and calcium signals. *Cell*. 1997;89(7):1145–1153.
21. Bernardi P, Petronilli V. The permeability transition pore as a mitochondrial calcium release channel: a critical appraisal. *J Bioenerg Biomembr*. 1996; 28(2):131–138.
22. Nagai T, Sawano A, Park ES, Miyawaki A. Circularly permuted green fluorescent proteins engineered to sense Ca2+. *Proc Natl Acad Sci U S A*. 2001; 98(6):3197–3202.
23. Altschuld RA, Hohl CM, Castillo LC, Garleb AA, Starling RC, Brierley GP. Cyclosporin inhibits mitochondrial calcium efflux in isolated adult rat ventricular cardiomyocytes. *Am J Physiol*. 1992; 262(6 pt 2):H1699–H1704.
24. Loupatatzis C, Seitz G, Schonfeld P, Lang F, Siemen D. Single-channel currents of the permeability transition pore from the inner mitochondrial membrane of rat liver and of a human hepatoma cell line. *Cell Physiol Biochem*. 2002;12(5–6):269–278.
25. Liu T, O'Rourke B. Regulation of mitochondrial Ca2+ and its effects on energetics and redox balance in normal and failing heart. *J Bioenerg Biomembr*. 2009;41(2):127–132.
26. Denton RM. Regulation of mitochondrial dehydrogenases by calcium ions. *Biochim Biophys Acta*. 2009; 1787(11):1309–1316.
27. Brandes R, Bers DM. Simultaneous measurements of mitochondrial NADH and Ca(2+) during increased work in intact rat heart trabeculae. *Biophys J*. 2002;83(2):587–604.
28. McCormack JG, England PJ. Ruthenium red inhibits the activation of pyruvate dehydrogenase caused by positive inotropic agents in the perfused rat heart. *Biochem J*. 1983;214(2):581–585.
29. Unitt JF, McCormack JG, Reid D, MacLachlan LK, England PJ. Direct evidence for a role of intramitochondrial Ca2+ in the regulation of oxidative phosphorylation in the stimulated rat heart. Studies using 31P n.m.r. and ruthenium red. *Biochem J*. 1989; 262(1):293–301.
30. Piao L, et al. The inhibition of pyruvate dehydrogenase kinase improves impaired cardiac function and electrical remodeling in two models of right ventricular hypertrophy: resuscitating the hibernating right ventricle. *J Mol Med*. 2010;88(1):47–60.
31. Nakayama H, et al. Ca2+- and mitochondrial-dependent cardiomyocyte necrosis as a primary mediator of heart failure. *J Clin Invest*. 2007;117(9):2431–2444.
32. Lehman JJ, Kelly DP. Gene regulatory mechanisms governing energy metabolism during cardiac hypertrophic growth. *Heart Fail Rev*. 2002;7(2):175–185.
33. Taegtmeyer H, Wilson CR, Razeghi P, Sharma S. Metabolic energetics and genetics in the heart. *Ann N Y Acad Sci*. 2005;1047:208–218.
34. Barger PM, Brandt JM, Leone TC, Weinheimer CJ, Kelly DP. Deactivation of peroxisome proliferator-activated receptor-alpha during cardiac hypertrophic growth. *J Clin Invest*. 2000;105(12):1723–1730.
35. Watanabe K, et al. Constitutive regulation of cardiac fatty acid metabolism through peroxisome proliferator-activated receptor alpha associated with age-dependent cardiac toxicity. *J Biol Chem*. 2000;275(29):22293–22299.
36. Leone TC, Weinheimer CJ, Kelly DP. A critical role for the peroxisome proliferator-activated receptor alpha (PPARalpha) in the cellular fasting response: the PPARalpha-null mouse as a model of fatty acid oxidation disorders. *Proc Natl Acad Sci U S A*. 1999; 96(13):7473–7478.
37. Cheng L, et al. Cardiomyocyte-restricted peroxisome proliferator-activated receptor-delta deletion perturbs myocardial fatty acid oxidation and leads to cardiomyopathy. *Nat Med*. 2004;10(11):1245–1250.
38. Yan J, Young ME, Cui L, Lopaschuk GD, Liao R, Tian R. Increased glucose uptake and oxidation in mouse hearts prevent high fatty acid oxidation but cause cardiac dysfunction in diet-induced obesity. *Circulation*. 2009;119(21):2818–2828.
39. Maillet M, Lynch JM, Sanna B, York AJ, Zheng Y, Molkentin JD. Cdc42 is an antihypertrophic molecular switch in the mouse heart. *J Clin Invest*. 2009; 119(10):3079–3088.
40. Picard M, et al. Resistance to Ca2+-induced opening of the permeability transition pore differs in mitochondria from glycolytic and oxidative muscles. *Am J Physiol Regul Integr Comp Physiol*. 2008;295(2):R659–R668.
41. Gabel SA, Walker VR, London RE, Steenbergen C, Korach KS, Murphy E. Estrogen receptor beta mediates gender differences in ischemia/reperfusion injury. *J Mol Cell Cardiol*. 2005;38(2):289–297.
42. De Windt LJ, Lim HW, Haq S, Force T, Molkentin JD. Calcineurin promotes protein kinase C and c-Jun NH2-terminal kinase activation in the heart. Cross-talk between cardiac hypertrophic signaling pathways. *J Biol Chem*. 2000;275(18):13571–13579.
43. Kettlewell S, Cabrero P, Nicklin SA, Dow JA, Davies S, Smith GL. Changes of intra-mitochondrial Ca2+ in adult ventricular cardiomyocytes examined using a novel fluorescent Ca2+ indicator targeted to mitochondria. *J Mol Cell Cardiol*. 2009;46(6):891–901.
44. Huang da W, et al. The DAVID Gene Functional Classification Tool: a novel biological module-centric algorithm to functionally analyze large gene lists. *Genome Biol*. 2007;8(9):R183.
45. Huang da W, Sherman BT, Lempicki RA. Systematic and integrative analysis of large gene lists using DAVID bioinformatics resources. *Nat Protoc*. 2009; 4(1):44–57.
46. Wilkins BJ, et al. Calcineurin/NFAT coupling participates in pathological, but not physiological, cardiac hypertrophy. *Circ Res*. 2004;94(1):110–118.